Geophys. J. Int. (2007) **170,** 1119–1128 doi: 10.1111/j.1365-246X.2007.03368.x

Size and duration of the high-frequency radiator in the source of the 2004 December 26 Sumatra earthquake

A. A. Gusev,[1,2] E. M. Guseva[2] and G. F. Panza[3]

[1] *Institute of Volcanology and Seismology, Russ. Ac. Sci.* 9 *Piip Blvd,* 683006 *Petropavlovsk-Kamchatskii, Russia. E-mail: gusev@emsd.iks.ru*
[2] *Kamchatka Branch, Geophys. Serice, Russ. Ac. Sci.,* 9 *Piip Blvd,* 683006 *Petropavlovsk-Kamchatskii, Russia*
[3] *University of Trieste, Department of Earth Sciences, via Weiss* 4, 34127 *and the Abdus Salam International Centre for Theoretical Physics – SAND group, Trieste, Italy*

Accepted 2007 February 5. Received 2006 December 19; in original form 2006 May 3

SUMMARY

We recover the gross space–time characteristics of high-frequency (HF) radiator of the great Sumatra-Andaman islands earthquake of 2004 December 26 ($M_w = 9.1$–9.3) using the time histories of the power of radiated HF *P* waves. To determine these time histories we process teleseismic *P* waves at 36 BB stations, using, in sequence: (1) bandpass filtering (four bands: 0.4–1.2, 1.2–2, 2–3 and 3–4 Hz); (2) squaring wave amplitudes, making 'power signals' for each band and (3) stripping the propagation-related distortion (*P* coda, etc.) from the power signal and thus recovering source time function for HF power. In step (3) we employ an inverse filter constructed from an empirical Green's function, which is estimated as the power signal from an aftershock. For each ray we thus obtain signals with relatively well-defined end and no coda. From these signals we extract: total duration (joint estimate for all four bands) and temporal centroid of signal power for each band. Through linear inversion, the set of duration values for a set of rays delivers estimates of the rupture stopping point and stopping time. Similarly, the set of temporal centroids can be inverted to obtain the position of the space–time centroid of HF energy radiator. The quality of inversion for centroid is acceptable for lower-frequency bands but deteriorates for higher-frequency bands where only a fraction of stations provide useful data. For the source length and duration the following joint estimates were obtained: 1241 ± 224 km, 550 ± 10 s. The estimated stopping point position corresponds to the northern extremity of the aftershock zone. Spatial HF radiation centroids are located at distances 350–700 km from the epicentre, in a systematic way: the higher is the frequency, the farther is the centroid from the epicentre. Average rupture propagation velocity is estimated as 2.25 km s^{-1}.

Key words: earthquake-source mechanism, rupture propagation, seismic coda, source time functions, subduction zone, waveform analysis.

INTRODUCTION

The inversion of seismograms to determine the source of the recent giant Sumatra-Andaman Islands earthquake of 2004 December 26 was a challenge, in particular because it is difficult to isolate *P* and *S* waves when the source duration is very long. To alleviate this problem one can use *P*-wave signal at high frequencies (HF signal, roughly, at frequencies f above 0.5 Hz) where it is relatively free from contamination by later phases (Lomax 2005; Ni *et al.* 2005). However, raw teleseismic high-frequency (HF) signals are always distorted by wave scattering along the propagation path. This distortion is well known as *P* coda. To analyse HF signal efficiently, one has to suppress this distortion. After such a correction, parameters of the HF radiator in the earthquake source can be determined. To perform both these steps consistently, the key point is to treat HF body wave as a random signal, and analyse its instant power, or squared amplitude. This approach, proposed by Gusev & Pavlov (1978), has been developed in the last decades both for teleseismic (Gusev & Pavlov 1991, 1998) and regional (Zeng *et al.* 1993; Kakehi & Irikura 1996; Nishmura *et al.* 1996) data. As usually the case with source studies, a number of assumptions are needed to permit a particular analysis. First of all, instead of the routine treatment of a source as an aggregate of elements whose *amplitudes* at the receiver are additive, we assume that such elements are spots generating statistically independent (uncorrelated) random HF signals, so that these signals are additive in terms of their *power* (measured by mean squared amplitude). Such a 'non-coherent' source is naturally described by space–time distribution of radiated energy per unit area and unit time, or, shortly, by its *luminosity* function. Therefore, space–time parameters of source luminosity function are what we seek for.

For a surface-focus event of considerable magnitude, one can assume its vertical dimensions negligible, and seek for luminosity distribution in 3-D ($x_1 \times x_2 \times t$). To analyse recorded signals, one must relate them to luminosity distribution over the source. We are interested here in the analysis of teleseismic *P* waves. For this kind of data, there is a considerable difference between the well-known case of medium and low-frequency waves, on one hand, and HF waves, on the other. In the former case, source signals, radiated along a certain ray arrives to a station with little contamination; and the corresponding Green's function (GF) consists of *P*, *pP* and *sP* pulses that are approximately delta-like. For the HF signal, however, scattering and conversion result in significant *P*-coda energy that complicates this clear picture. In addition, it is impossible to sort out *P*, *pP* and *sP* contributions within the complete HF signal of an earthquake of considerable magnitude. To overcome this problem, Gusev & Pavlov (1991) proposed to employ the additivity of power and to deconvolve the recorded power signal using an empirical GF for power estimated from the record of an aftershock. For the common case of sources of earthquakes with $M \geq 7$–7.5, when the vertical extent of the source is small as compared to horizontal one, the local mean source depth does not change significantly along the source length. In our case, this approach is particularly acceptable because in the deconvolution we use a rather big time step. The spectral-domain deconvolution of Gusev & Pavlov (1991) was noisy; it was then radically stabilized by adding positivity constraint (Gusev & Pavlov 1998).

After the reconstruction of the source power pulse, one can analyse signals over the focal sphere to deduce the space–time structure of the source. In the following we confine our study to two (vectorial) source parameters: (1) spatio-temporal centroid and (2) rupture stopping point/moment. Generally, the determination of the stopping point is not a well-posed problem. However it becomes better defined for a narrow fault with purely unilateral rupture propagation, and, fortunately, this is approximately the case for the 2004 December 26 event. Source centroid, on the contrary, is a model-independent entity, and its recovery is a well-posed problem.

METHOD

We give here a compressed description only; see Gusev & Pavlov (1988, 1991) for more details. Let us consider first the case of a homogeneous scattering medium. Let a finite planar source Σ of diameter D with area element $\mathrm{d}\Sigma$ be described, for a certain frequency band ($f_0 - \Delta f/2, f_0 + \Delta f/2$) by source luminosity function $L(\boldsymbol{x}, t, f_0\ \Delta f)$. With respect to time argument t, $L()$ is assumed finite, being nonzero only over the interval $[0, T]$. In the following we assume both central frequency f_0 and bandwidth Δf fixed, and thus omit these arguments. Let the hypocentre be located within Σ and be the origin of the Cartesian reference system, and the zero-time reference to coincide with the source nucleation time (=origin time). Let us consider a far-field receiver located at $\boldsymbol{y}$, on a ray $\boldsymbol{r}$ ($\|\boldsymbol{r}\| = 1\|$) at a distance $\|\boldsymbol{y}\| = R \gg D$. We introduce the GF for power $G_0(\boldsymbol{y}, t|\boldsymbol{x})$ as the power that reached the receiver at $\boldsymbol{y}$, propagating from a unit source area located at $\boldsymbol{x}$, produced by a spike-like luminosity burst at this area, with unit integral, fired at $t = 0$. We assume, further, that the dependence of $G_0(\boldsymbol{y}, t|\boldsymbol{x})$ on the argument $\boldsymbol{x}$ is weak, and can be ignored; thus we can write $G(\boldsymbol{y}, t)$ instead of $G_0(\boldsymbol{y}, t|\boldsymbol{x})$. Informally, we assume that the *mean* scattering response of the medium is the same for any $\mathrm{d}\Sigma$. Now, the contribution from $\mathrm{d}\Sigma$ to body wave power at $\boldsymbol{y}$ can be written as a convolution over time:

$$\mathrm{d}W(\boldsymbol{y}, t) = \int_{-\infty}^{\infty} G(\boldsymbol{y}, t - \tau + \boldsymbol{x} \cdot \boldsymbol{r}/c) L(\boldsymbol{x}, \tau) \mathrm{d}\tau, \tag{1}$$

where c is the body wave velocity. When there is no scattering, $G(\boldsymbol{y}, t)$ reduces to $(\Re /R)^2\, \delta(t - R/c)$ where $\Re$ is the point-source radiation pattern. Integrating (1) over Σ one obtains:

$$W(\boldsymbol{y}, t) = \int_{\Sigma} \int_{-\infty}^{\infty} G(\boldsymbol{y}, t - \tau + \boldsymbol{x} \cdot \boldsymbol{r}/c) L(\boldsymbol{x}, \tau) \mathrm{d}\tau \mathrm{d}\Sigma. \tag{2}$$

The order of integration in (2) can be changed, to result in:

$$W(\boldsymbol{y}, t) = \int_{-\infty}^{\infty} \left[\int_{\Sigma} L(\boldsymbol{x}, t - \tau + \boldsymbol{x} \cdot \boldsymbol{r}/c) \mathrm{d}\Sigma \right] G(\boldsymbol{y}, \tau) \mathrm{d}\tau. \tag{3}$$

The outer convolution in (3) can be inverted if one knows $G(\boldsymbol{y}, t)$ and can construct the corresponding deconvolution operator. Let its time-domain representation be $G^{-1}(\boldsymbol{y}, t)$. The result of deconvolution is the power signal in a non-scattering medium:

$$W_0(\boldsymbol{y}, t) = G^{-1}(\boldsymbol{y}, \cdot)\, W(\boldsymbol{y}, \cdot) = \int_{\Sigma} L(\boldsymbol{x}, t + \boldsymbol{x} \cdot \boldsymbol{r}/c) \mathrm{d}\Sigma. \tag{4}$$

In this compact derivation we passed over some important points that must be mentioned. First, the source element $\mathrm{d}\Sigma$ of non-coherent radiator cannot be infinitesimally small: its diameter cannot be smaller than the 'source correlation radius' (Gusev 1983), order of or larger than half wavelength; thus the integral representation (2) is not a completely accurate one. Second, when considering $L()$, $G()$ and $W()$ functions, one must distinguish between mean (ensemble average) power time histories and observed realizations (sample functions). Eqs (1–4) are written for ensemble averages; hence, when they are used for practical inversion, one inevitably meets with a significant fluctuational noise, to be discussed separately. Third, the value of bandwidth Δf is not arbitrary: it must be sufficiently large to ensure inequality $1/\Delta f \ll T$ (where $1/\Delta f$ can be treated as signal correlation time).

With $W_0(\boldsymbol{y}, t)$ known at several rays, one can recover the parameters of the source space–time structure. In particular, it is interesting to determine the centroid of $L(\boldsymbol{x}, t)$, or 4-vector of normalized order 1 power moments $\{M_t\, M_1\, M_2\, M_3\}$ (see e.g. Gusev & Pavlov 1988):

$$M_t = F(L, t, 1)/F(L, 1, 0);$$

$$M_i = F(L, x_i/c, 1)/F(L, 1, 0), \tag{5}$$

where

$$F(g, z, n) \stackrel{\text{def}}{=} \int_{-\infty}^{\infty} \int_{\Sigma} g(x, t) z^n \mathrm{d}\Sigma \mathrm{d}\tau.$$

To determine the source centroid, one solves the linear system of equations:

$$M_t - (1/c)(r_{1k} M_1 + r_{2k} M_2 + r_{3k} M_3) = e_k, \tag{6}$$

where k is the number of a station/ray/receiver, $k = 1, 2, \ldots N$, and

$$e_k = \frac{\int W_0(t) t \mathrm{d}t}{\int W_0(t) \mathrm{d}t} \tag{7}$$

is the temporal centroid of the observed body wave power pulse at the kth receiver.

The same eq. (6) holds also for the space–time position (4-vector) of any common feature discernible on many records and caused by a certain individual event of the fault motion, if this event is definitely localized in space–time. In this case, e_k must be replaced by the delay of the feature with respect to the first arrival. Traditionally, this approach has been widely applied to 'starting phases', 'stopping

phases' and 'subevents'. In the following, we shall use total signal duration $T_{\rm fin}$ to determine in this way the 4-vector of the stopping point of the rupture; we denote its space–time location as $\{F_t\, F_1\, F_2\, F_3\}$ or $\boldsymbol{F}$.

Let us now pass to the case of the real Earth. We introduce the coordinates$\{x, y, z\}$ along N, E and Z directions. When geometrical non-linearity can be neglected, the first two r_{ik}/c coefficients in eq. (6) can be replaced by the corresponding travel time derivatives $\{{\rm d}T/{\rm d}x = \cos(Az){\rm d}T/{\rm d}\Delta {\rm d}T/{\rm d}y = \sin(Az){\rm d}T/{\rm d}\Delta\}$. This is applicable in the case of a small source size. However, the actual source size of the 2004 December 26 event is too large to blindly rely on linearization. Therefore, an appropriate non-linear least-squares procedure has been designed and used in the further analysis. (The actual gain in accuracy related to this refinement is in fact small.) The size of the source in question along z axis is relatively small; therefore, we shall use the constraint $M_3 = M_z = 0$ in the following, reducing the number of unknowns in eq. (6) to three. The small relative source size along z is an additional argument to ignore the dependence of $G_0(\boldsymbol{y}, t|\boldsymbol{x})$ on $\boldsymbol{x}$.

For the case of a homogeneous scattering medium, we could believe that the GF $G_0(\boldsymbol{y}, t|\,\boldsymbol{x})$ is merely a combination of the direct body wave and scattered coda. For the real Earth, however, $G_0(\boldsymbol{y}, t|\,\boldsymbol{x})$ also includes deterministic pP, sP and similar phases. This means that to extract the 'clean' $G_0(\boldsymbol{y}, t|\,\boldsymbol{x})$ from observations we must use an aftershock with moment tensor orientation and depth preferably similar to that of the main shock. Possible biases related to non-identical moment tensor orientations of main shock and aftershock (that, in theory, may result in variations of relative amplitudes of P, pP and sP phases) were ignored, in particular because of the known inefficiency of standard radiation pattern factors to predict the mentioned relative amplitudes for HF P waves of large earthquakes. The aftershock used was selected to have the hypocentre depth near to the main shock centroid depth (30 km), and to represent a low-angle thrust whose strike is only 35° different from that of the main shock. These choices are however not very critical in our case since to stabilize the deconvolution we shall use a rather large time step, of 10 s. With such a time step, most differences in time delays of P, pP and sP among source elements located at various depths are smeared because the entire P-wave group is represented by a one or two samples of the time history.

According to the described approach, the following processing algorithm has been developed. A P wave record is corrected for the instrument and, approximately, for path attenuation, and converted to acceleration signal. We use acceleration signal instead of velocity signal (that would be needed in a more strict analysis of wave power) because we are interested in the maximum suppression of fluctuational noise. See Appendix for the discussion of this point. The acceleration signal is passed through four passband filters 0.4–1.2, 1.2–2, 2–3 and 3–4 Hz, identified in the following by their central frequencies 0.8, 1.6, 2.5 and 3.5 Hz. In each band, the 'raw' signal power $A_{\rm rs}(t) \equiv a^2_{\rm rs}(t)$ is estimated as squared modulus of analytical signal: $a^2_{\rm rs}(t) = u^2(t) + ({\rm H}[u(t)])^2$ (where H[] denotes Hilbert transform and $u(t)$ is the filtered acceleration). A similar operation is applied to a segment of noise before P-wave arrival, and the average power of noise, $A_{n,av} = \overline{A_n(t)}$ is subtracted from the samples of 'raw' signal power, to obtain an initial signal power $W(t)$. The samples of $W(t)$ are then averaged twice, over intermediate and large time bins. In the first averaging we use a bin size ${\rm d}t_1 = 1$ s; this averaging generates a jagged envelope signal that is used to set, interactively, the P wave onset time. In the second averaging, with bin size ${\rm d}t_2 = 10$ s, a signal representation is obtained that is suitable for the deconvolution procedure. This ${\rm d}t_2$ value has been selected by trial and error to provide a trade-off between temporal resolution and stability of deconvolution. During such a processing, first only binning and averaging was applied to data, similarly for main shock and aftershock. After that, main shock signal was slightly smoothed by finite impulse response filter with weights $\{1, 1, 1\}$; this operation somewhat reduces the noise of the subsequent inversion.

When the above processing is completed for the main shock and the aftershock, deconvolution is performed. It consists of the numerical solution of the convolution equation:

$$C_1 W_1(\cdot) * W_{\rm a}(\cdot) = W_{\rm m}(\cdot), \tag{8}$$

where $W_{\rm m}(t)$ and $W_{\rm a}(t)$ are known main shock and aftershock time functions at a station, $W_1(t)$ is an unknown source signal for the main shock, and $C_1 = 1/\int W_{\rm a}(t){\rm d}t$ is a scale coefficient. Entire combination $C_1 W_1(\cdot)$ is found in deconvolution. The unknown C_1 coefficient is inessential because it cancels when e_k is calculated through eq. (7). Solution is sought for in time domain using non-negative least squares procedure (NNLS) of Lawson and Hanson.

Although NNLS stabilizes inversion significantly, certain noise persists that hinders reliable determination of $T_{\rm fin}$ separately for each band. Therefore, we determine $T_{\rm fin}$ of a station k by joint visual analysis of all estimates of $W_1(t)$ time histories (of four or less bands). With $T_{\rm fin}$ known, centroid times e_k are determined for each band, denoted $e_k{}^{(0.8)}$ $e_k{}^{(1.6)}$, etc. The degree of certainty of the result was rated as 'good', 'acceptable', 'doubtful' or 'to discard', and corresponding weights, equal to 1.0, 0.5, 0.05 or 0.0, were associated with the obtained estimates in the further processing.

DATA SELECTION, PROCESSING AND ITS RESULTS

About 50 P-wave records of the main shock [2004 December 26 at 005853, instrumental hypocentre 3.30°N, 95.98°E, depth 30 km,

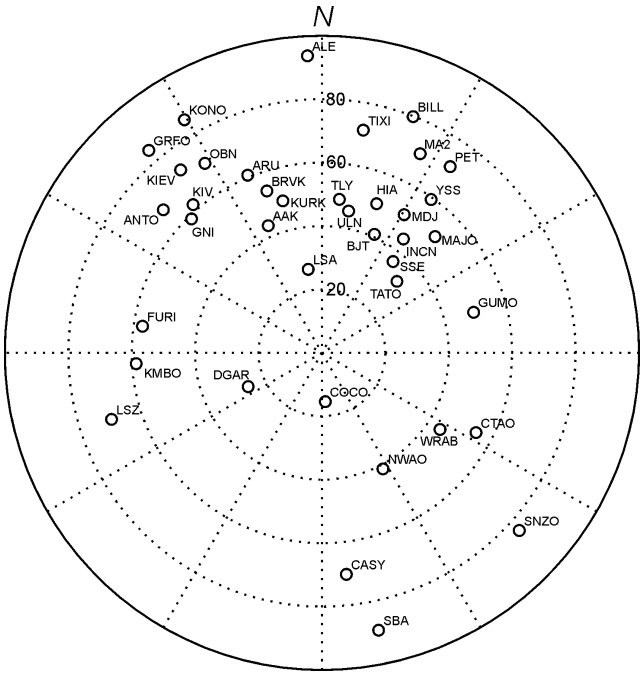

Figure 1. Distribution of used stations over azimuth and epicentral distance.

M_w(HRV) = 9.0] on BHZ channels of GDSN stations have been acquired through IRIS DMS data centre. In selecting data we tried to avoid severely non-uniform data coverage over a focal sphere, and also to limit the number of coastal stations with, usually, low signal-to-noise (S/N) ratio for the higher-frequency bands. An unexpectedly high number of stations have shown significantly distorted HF signal, with isolated or periodic spikes and pulses, HF noise bursts and other peculiarities of probably instrument/recorder origin. The 39 better-quality records were selected for further analysis (Fig. 1). More problems appeared when selecting aftershock records. Recorder problems are rare in this case, but noise levels are too high in many cases, especially at higher frequencies. Some larger-magnitude aftershocks were discarded as having too long source duration (double shocks?). Among the data within the optimal magnitude span, that is, of $m_b = 5.8$–6.5, no event was acceptably recorded on all stations simultaneously. Abstractly speaking, there is the possibility to combine the results from the deconvolution performed using different aftershocks for different stations. We found that even in this lower-magnitude range, and in cases of matching depth and moment tensor orientation, the event duration can vary significantly from one aftershock to another. (We ascribe this observation, conceivably, to location-dependent water column resonances/*PwP* phases.) Therefore, mixing estimates obtained using different aftershocks would add a significant and incontrollable noise into inversion. Our way to overcome this difficulty is primitive. We selected the aftershock of 2005 February 26 at 12 hr 56 m, hypocentre 2.91°N, 95.59°E, depth 36 km, M_w(HRV) = 6.7, m_b = 6 as providing the best trade-off between completeness of station set and limited duration of the *P*-wave group. In cases when the record quality was unacceptable (S/N ratio is too high), we construct the inverse filter by the record of the same aftershock, but from another station. In all such cases, we use the low-noise record of KURK, with the value of duration that is intermediate among various stations. To illustrate possible errors related to such a replacement, in Fig. 2 we compare 29 $e_k^{(0.8)}$ and 30 $T_{\mathrm{fin},k}$ values obtained using the 'own' aftershock record at each station, against the case when the aftershock record from KURK was used instead. This comparison is presented for stations where the aftershock was recorded

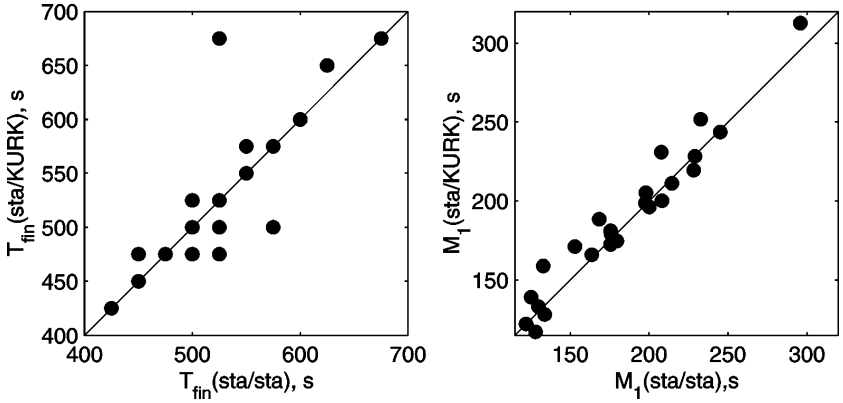

Figure 2. Illustration of the limited bias introduced by the replacement, in the solution of eq. (7), of the aftershock record from the same station as one recorded the main shock, with a similar record by the station KURK, for the case of the aftershock 2006 February 26. Abscissa: correct estimate of $T_{\mathrm{fin},k}$ and $e_k^{(0.8)}$; ordinate: estimate obtained through the replacement.

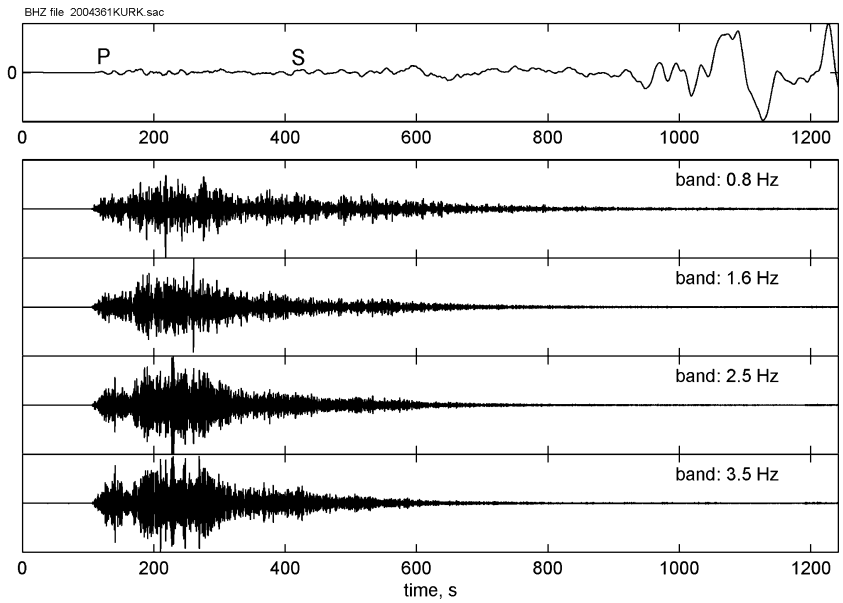

Figure 3. Attenuation-corrected main shock signal at KURK: displacement (upper trace) and four band-filtered acceleration traces. The time reference is arbitrary.

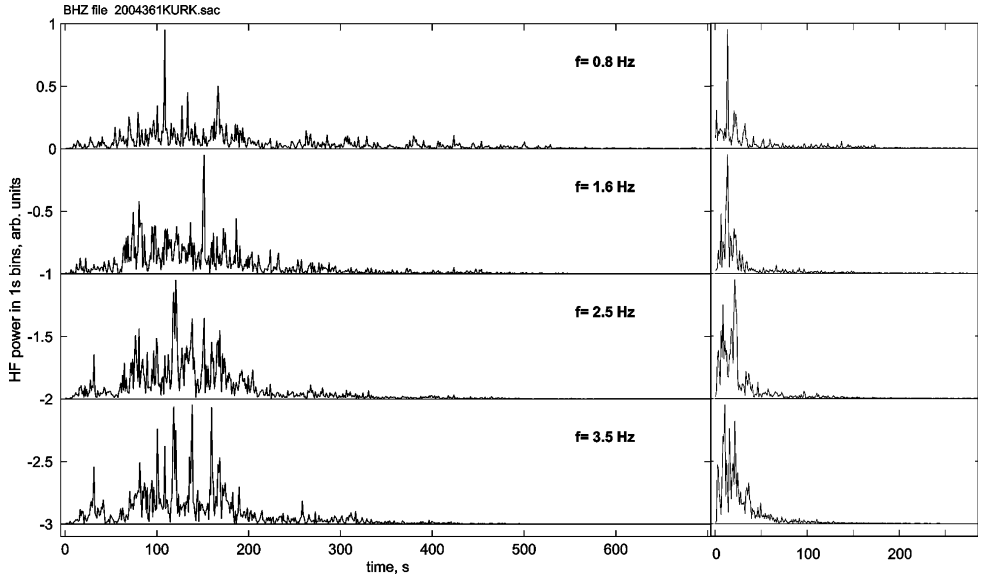

Figure 4. HF power signals (energy in 1-s bins) for bandpass-filtered acceleration signals at KURK, for the main shock (left) and aftershock 2005 February 26 (right). The time count is from onset time.

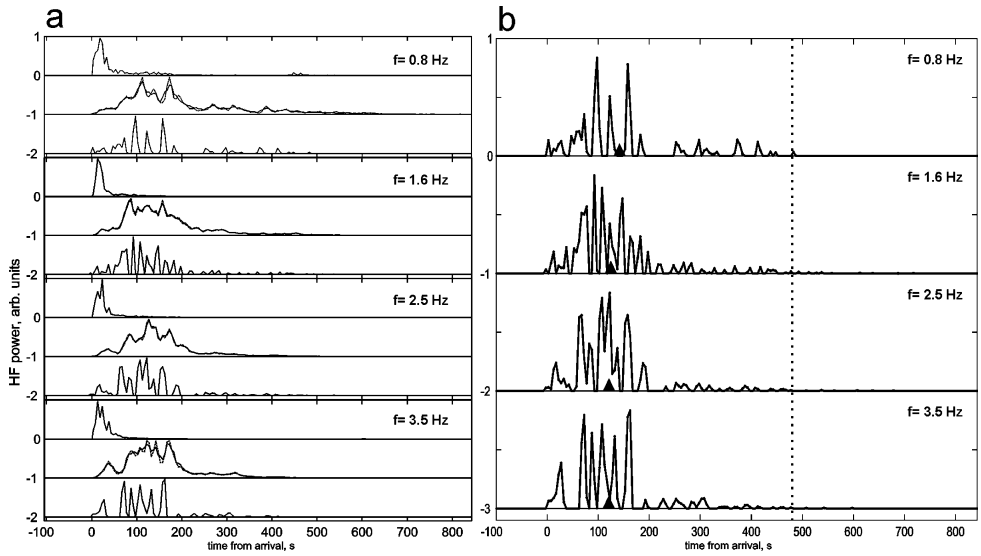

Figure 5. Deconvolution procedure for the power signals at KURK (Fig. 4), averaged over 10-s bins. (a) four boxes are shown, one for each of the four frequency bands; a box contains three curves: upper curve—aftershock signal W_a (t), middle curve—main shock signal W_m (t) (solid) and, overlapped on it, the convolution $W_a() * CW_1()$ (dashes, mostly difficult to notice), lower curve—deconvolved ('cleaned') main shock signal $W_1(t)$. (b) $W_1(t)$ signals in more detail. Triangles marks centroids e_k for each band, and the vertical dashed line marks the joint end time $T_{\mathrm{fin},k}$.

acceptably. One can see that the distortion is limited. In numerical terms, rms relative error related to such replacement was estimated to be about 7 per cent both for $T_{\mathrm{fin},k}$ and for $e_k^{(0.8)}$ (for other bands, deviations are similar). This suggests that for the other 10 or 11 stations, where we do not have usable records of the same aftershock, related distortion is, probably, tolerable.

In Fig. 3, we illustrate our processing procedure. One can see band-filtered HF signals whose duration is much longer than *S–P* time. Envelope shapes vary from band to band, justifying the independent processing of bands. An accurate determination of the stopping point of the record is impossible (as usual) because of the presence *P* coda.

In Fig. 4, we show the example power signals of the main shock and of the aftershock with 1 s resolution. In Fig. 5, for each frequency band, the same signals are shown summed over 10-s bins, accompanied by the results of deconvolution ($W_1(t)$, in arbitrary units). The positivity constraint imposed during deconvolution might result in an imperfect fit of 'observed' $W_m(t)$ and 'fitted' $W_{mf}(t) = CW_1(.) * W_a(.)$ signals. In Fig. 5(a) in the same strip of the plot, two traces are plotted: observed $W_m(t)$ and fitted $W_{mf}(t)$; one can see that visually they are almost indistinguishable, showing quite acceptable fit. Another important observation is that the lowermost-frequency band (0.8 Hz) does not show any additional delay as compared to other bands, thus indicating that contribution of *S*-wave energy to the analysed traces is negligible. Actually, the opposite is seen: deconvolved signal durations at the 0.8-Hz band are slightly shorter than those at other bands for a large fraction of stations.

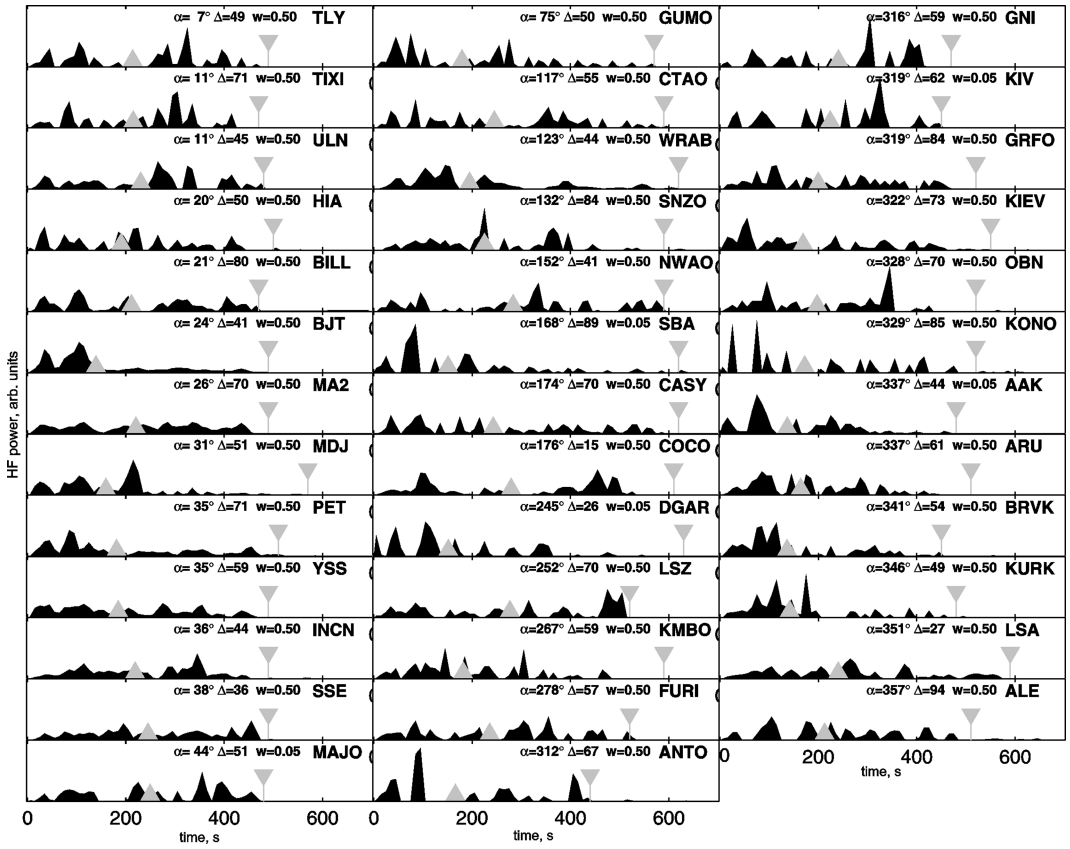

Figure 6. Recovered source signals of HF power for the 1.6 Hz band, for all stations. Triangle is centroid, and inverted triangle is the end time. α,Δ and w denote azimuth, epicentral distance and weight. No trace is shown for station TATO, that got zero weight for the 1.6 Hz band.

Table 1. Examples of temporal parameters derived from power signals of individual stations.

Station	Az (°)	Δ (°)	dT/dΔ (s deg^{-1})	$T_{\mathrm{fin},k}$ (s)	$e_k^{(0.8)}$ (s)	$e_k^{(1.6)}$ (s)	$e_k^{(2.5)}$ (s)	$e_k^{(3.5)}$ (s)
TIXI	10.5	71	6.04	440	199	196	211	202
ULN	10.6	45	7.92	480	189	151	164	–
BILL	21.1	79	5.41	460	163	146	142	165
CTAO	117.3	54	7.25	630	235	226	274	279
WRAB	122.9	44	8.00	620	172	210	234	256
SNZO	131.9	83	5.11	640	225	199	221	230
SBA	168.4	89	4.68	630	141	153	–	–
LSA	350.6	26	9.01	560	207	167	194	216

Az—azimuth; Δ—epicentral distance; dT/dΔ(s deg^{-1})—P traveltime derivative. (–) means the lack of an estimate because of insufficient S/N ratio or dirty data. For other denotations see text.

All $W_1(t)$ signals for the 1.6 Hz band are shown on Fig. 6. Despite considerable scatter, systematic variation of $T_{\mathrm{fin},k}$ and e_k with azimuth is seen, indicating Doppler effect from the approximately northward rupture propagation.

Sets of $T_{\mathrm{fin},k}$ and e_k (see examples in Table 1) were processed by non-linear least squares as mentioned above, to result in vectors: $\{F_t\ F_x\ F_y\}$ or $\boldsymbol{F}$ for stopping time-location, and $\{M1_t\ M1_x\ M1_y\}$ or $\boldsymbol{M1}$ for centroid (four $\boldsymbol{M1}$ estimates, one per band). Examples of the least squares fit of $T_{\mathrm{fin},k}$ and e_k data can be seen in Fig. 7, for $\boldsymbol{F}$ vector and for the two most reliable centroid vectors.

The results of the inversion described above are given in Table 2 under the subheader 'Data set A'. Each line of estimates of $\boldsymbol{F}$ and $\boldsymbol{M1}$ vectors in Table 2 is followed by a line of their standard deviations determined from linearized least squares (and by propagation of errors when needed). In the header, N is the number of stations; columns $[]_t$, $[]_N$ and $[]_E$ contain temporal, N and E components of an estimated vector, correspondingly. In a similar way, the columns $[]_L$, $[]_{Az}$ and $[]_V$ contain the estimates for the length of the spatial part of the vector, its azimuth, and propagation velocity. In the side-heading, a superscript denotes the frequency band. The graphical representation of the spatial part of these vectors is given in Fig. 8.

The results are consistent and all indicate NNW direction of rupture propagation. For an ideal case of constant luminosity per km of length, the velocity estimate associated with $\boldsymbol{M1}$ must be about twice the true velocity associated with $\boldsymbol{F}$; this is roughly true for rupture velocity estimates. A significant fact is rather limited accuracy of the spatial parts of $\boldsymbol{M1}$ and $\boldsymbol{F}$ vectors as manifested in considerable error estimates. For the 2.5 Hz and especially for 3.5 Hz band, errors

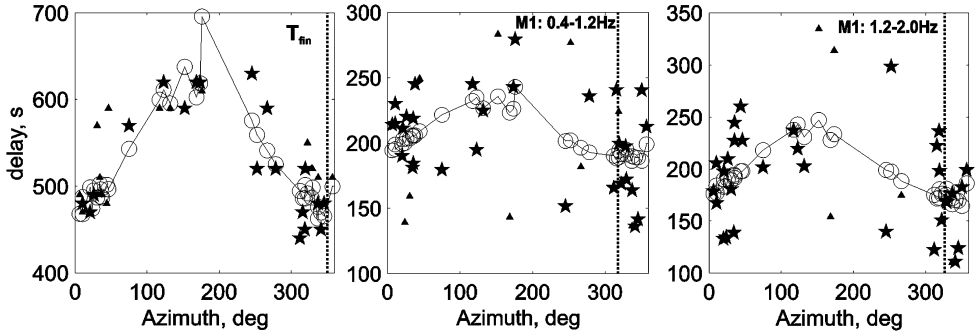

Figure 7. Illustration of the quality of fit of observed delays $T_{\mathrm{fin},k}$ and e_k by least squares (eq. 6), while determining $\boldsymbol{F}$, $\boldsymbol{MI}^{(0.8)}$ and $\boldsymbol{MI}^{(1.6)}$. Circles: calculated values, pentagrams: observed values with weights 0.5 and more and triangles: same data with lesser weight. The vertical line marks the azimuth obtained in the inversion.

Table 2. Solutions for space–time vectors of source parameters, for the basic (A) and additional data sets.

Parameter	N	$[]_t$ (s)	$[]_N$ (km)	$[]_E$ (km)	$[]_L$ (km)	$[]_{Az}$ (°)	$[]_V$ (km s^{-1})
				Data set A (basic)			
$\boldsymbol{F}$	37	550	1221	−217	1241	349	2.25
$\sigma(\boldsymbol{F})$		10	218	231	224	10	0.41
$\boldsymbol{MI}^{(0.8)}$	38	210	261	−239	354	317	1.68
$\sigma(\boldsymbol{MI}^{(0.8)})$		10	189	235	213	34	1.01
$\boldsymbol{MI}^{(1.6)}$	36	206	467	−306	559	326	2.71
$\sigma(\boldsymbol{MI}^{(1.6)})$		16	317	285	301	30	1.48
$\boldsymbol{MI}^{(2.5)}$	26	215	616	−375	721	328	3.34
$\sigma(\boldsymbol{MI}^{(2.5)})$		17	331	369	350	27	1.64
$\boldsymbol{MI}^{(3.5)}$	18	220	538	−451	702	320	3.19
$\sigma(\boldsymbol{MI}^{(3.5)})$		25	553	627	591	48	2.71
				Data set B			
$\boldsymbol{F}$	30	547	1227	−160	1237	352	2.25
$\sigma(\boldsymbol{F})$		12	260	273	266	12	0.48
$\boldsymbol{MI}^{(0.8)}$	29	212	213	−269	344	308	1.62
$\sigma(\boldsymbol{MI}^{(0.8)})$		12	226	277	253	42	1.19
$\boldsymbol{MI}^{(1.6)}$	28	209	477	−329	579	325	2.76
$\sigma(\boldsymbol{MI}^{(1.6)})$		19	392	346	370	36	1.78
$\boldsymbol{MI}^{(2.5)}$	18	211	646	−560	855	31	4.04
$\sigma(\boldsymbol{MI}^{(2.5)})$		22	393	475	436	32	2.11
$\boldsymbol{MI}^{(3.5)}$	10	194	−55	−1517	1518	26	7.80
$\sigma(\boldsymbol{MI}^{(3.5)})$		41	855	1096	982	53	5.32
				Data set C			
$\boldsymbol{F}$	39	558	1170	−174	1183	351	2.12
$\sigma(\boldsymbol{F})$		10	212	231	222	10	0.39
$\boldsymbol{MI}^{(0.8)}$	39	203	250	−131	282	332	1.38
$\sigma(\boldsymbol{MI}^{(0.8)})$		10	191	237	215	43	1.06
$\boldsymbol{MI}^{(1.6)}$	38	217	739	−439	860	329	3.96
$\sigma(\boldsymbol{MI}^{(1.6)})$		12	245	254	249	16	1.17
$\boldsymbol{MI}^{(2.5)}$	38	231	891	−485	1015	331	4.38
$\sigma(\boldsymbol{MI}^{(2.5)})$		14	287	257	272	15	1.20
$\boldsymbol{MI}^{(3.5)}$	35	234	908	−469	1022	332	4.37
$\sigma(\boldsymbol{MI}^{(3.5)})$		13	266	252	259	14	1.13
				Data set D			
$\boldsymbol{F}$	19	519	1133	−432	1213	339	2.33
$\sigma(\boldsymbol{F})$		11	240	317	281	13	0.54
$\boldsymbol{MI}^{(1.6)}$	20	187	860	−114	868	352	4.63
$\sigma(\boldsymbol{MI}^{(1.6)})$		15	340	415	379	25	2.06
				Data set E			
$\boldsymbol{F}$	39	560	1013	−186	1030	349	1.83
$\sigma(\boldsymbol{F})$		14	276	370	327	18	0.58

Symbols $[]_t$, $[]_N$, $[]_E$, etc. denote a particular component of a vector, for vectors $\boldsymbol{F}$, $\boldsymbol{MI}^{(0.8)}$, etc.
Symbols $[]_L$, $[]_{Az}$, $[]_V$, etc. denote length, azimuth and velocity derived from these components.

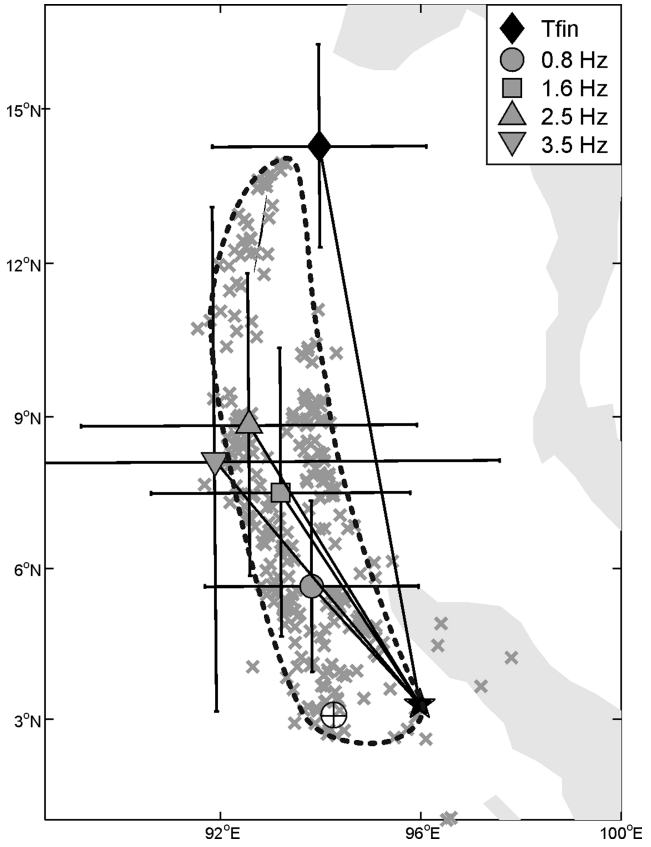

Figure 8. Locations for the stopping point and centroids for four bands. Star is the main shock hypocentre/nucleation point. Grey × marks are aftershocks of the first 25 hr, and the bold dash outline depicts the hypothetic source area consistent with these data. A cross around a marker depicts 1σ error bounds obtained in the LS inversion. The ⊕ symbol denotes Harvard CMT position for a single point source.

are particularly large; this is caused by almost complete lack of data at the southern azimuths, combined with the reduced total number of usable stations.

To understand reliability of the described results, a few more inversions have been done in addition to the already described case A. They used other variants of input data set, denoted by letters B, C, D and E. To form Data set B, we excluded from Data set A all cases when we used 'alien' aftershock record of KURK for deconvolution. In Data set C, conversely, all 39 available main shock traces were processed using the same aftershock record of KURK. One can see that with Data set B, the expected errors of results increased significantly, in particular for higher-frequency bands, but the estimates for $\boldsymbol{M1}$ at two lower-frequency bands, and for $\boldsymbol{F}$ vector are quite stable. The same three groups of estimates keep being stable also for Data set C.

In Data set D, deconvolution was based on the aftershock records of the event of 2005 January 1 (06 hr 25 m, $m_b = 6.0$), always using the 'own' aftershock record for each station. In this case, results were much less stable because of insufficient data volume. We show only result for $\boldsymbol{F}$ and $\boldsymbol{M}^{(1.6)}$ vectors, obtained with maximum data volume of 19 and 20 deconvolved records.

Creating Data set E we used the same initial data as with Data set A, but instead of time-domain deconvolution with NNLS procedure, more primitive approach was applied, by deconvolution through spectral division (stabilized by 'water level' of 3 per cent of spectral maximum). In this case, many estimates of e_k were evidently unreliable for all bands, and meaningful inversion was not possible. However, many $T_{\mathrm{fin},k}$ estimates looked more or less acceptable, and, when used in inversion, resulted in quite consistent $\boldsymbol{F}$ vector estimate, as given in Table 2. The results of four parallel inversions generally support our choice of processing procedure.

ANALYSIS OF RESULTS AND DISCUSSION

Comparing results obtained using data sets A–E one can see that the estimates based on vector $\boldsymbol{F}$ are most stable, especially the estimate of rupture duration. The estimates of source total length and orientation are also relatively stable. Generally, the number of stations is the most critical parameter: when this number is less than 30, the quality of estimates significantly deteriorates. Using NNLS deconvolution was found to be very important for obtaining reliable results.

The most clear qualitative result is the reasonable match between our estimate for the stopping point of the rupture, and the northern extremity of the 25-hr aftershock cloud. Our estimate for the source length is about 1250 km.

As for the position of centroids, one can notice certain mismatch between centroids for different frequency bands. This mismatch seems to be a real feature of the HF radiator. Another feature that can be deduced from comparing $M1_L$ and F_L values is the asymmetrical position of the centroid for 0.8 Hz with respect to the middle of the rupture length, indicating enhanced luminosity of the southern half of the fault for this band. For higher frequencies, such a clear asymmetry is not seen.

The temporal parameters of the HF radiator are determined with high accuracy. The estimate of full duration F_t is about 550 s. True duration values are insignificantly larger because deconvolution slightly squeezed the signals, by half-duration of the aftershock. Somewhat unexpected is the relatively low accuracy of the estimates of stopping point position and especially of spatial centroid, attained in the presented inversion. Two causes can be imagined for this problem, and both deserve analysis in a further study: the already mentioned fluctuational noise, and incomplete incoherency of radiation.

Several rupture size and duration estimates have been published for the 2004 December 26 event. We report, for comparison, the relevant ones in Table 3. A reasonable match for the length estimate is seen. The estimates for the position and delay of the source centroid are compiled in Table 4. The initial Harvard CMT estimate of the seismic moment centroid suggests a systematic shift of the centroid position with increasing frequency. Our own estimates of the centroid position for various frequencies show the same tendency. Comparing centroid positions for 0.8 and 2.5 Hz bands, in particular, one can derive from Table 2 that the significance level for the hypothesis $M1L_{0.8} < M1L_{2.5}$ is about 10 per cent. However, the revised estimate of the seismic moment centroid by Tsai *et al.* (2005), as well as the point estimate of Stein & Okal (2005) makes the idea of systematic change of centroid position with frequency less certain.

CONCLUSION

Using deconvolved time histories of the seismic HF power radiated to different directions by the source of the 2004 December 26 Sumatra-Andaman earthquake we successfully determined the positions of the stopping point and also centroids for the HF radiator in the source of this earthquake for four frequency bands. The

Table 3. Various estimates for the size and duration of the rupture of the 2004 December 26 event.

L (km)	Duration (s)	V_{rup} (km s^{-1})	Wave type	Comment	Reference
1200–1300[a]	575–625		*SH*, Raleigh	Duration from Fig. 6	Ammon *et al.* (2005)
1300[a]	≈480	2.8	*P* (0.2–1 Hz)	Local array analysis,	Ishi *et al.* (2005)
1150	480–500	2.3–2.7	BB *P*	Local array analysis	Krueger & Ohrnberger (2005)
1235	515	2.7 ⇒ 2.5 ⇒ 2.0	*T* phase, 1–100 Hz	Local array analysis	Guilbert *et al.* (2005)
1200	480	2.8 ⇒ 2.1	*T* phase, 1–100 Hz	Local array analysis	Tolstoy & Bohnenstiehl (2005)
1200	500	2.5	HF *P* (2–3 Hz)	Stopping point[b]	Ni *et al.* (2005)
1100 ± 300	560		HF *P* (≈1 Hz)	90 per cent stopping point	Lomax (2005)
1241 ± 224	550	2.25	HF *P* (0.4–3 Hz)	Stopping point	This study

[a]Along a curved fault trace.
[b]Endpoint of the envelope of HF *P* waves, picked by eye.

Table 4. Various estimates for the spatial and temporal centroid of the 2004 December 26 event.

N Latitude (°)	Delay (s)	Wave type	Comment	Reference
7		Normal modes		(Stein & Okal (2005)
3.1	139	Mantle waves	Standard CMT solution	www.seismology.harvard.edu
6.6	214	Mantle waves	Average over 5 subsources	Tsai *et al.* (2005)
[4–5]	[150–200]	*SH*, Raleigh, LF		Ammon *et al.* (2005)
[6]	[250–270]	*P* (0.2–1 Hz)	Regional array analysis,	Ishi *et al.* (20050
[6]	[200–270]	BB *P*	Local array analysis	Krueger & Ohrnberger (2005)
[6.5]	[160]	*T* phase, 1–100 Hz	Local array analysis	Tolstoy & Bohnenstiehl (2005)
[6–7]	[150–180]	*T* phase, 1–100 Hz	Local array analysis	(Guilbert *et al.* (2005)
5.5 (0.4–1.2 Hz)	215	HF *P*		This study
7.5 (1.2–2 Hz)				
8–9 (2–4 Hz)				

In brackets are our rough estimates based on plotted slip and power distributions in the sources listed.

results confirm the earlier estimates of source size (1200–1300 km) and duration (around 550 s). The approach to data analysis that uses 'cleaning' HF *P*-wave power signal by suppressing scattered-wave distortions and then making inversion using many rays proved to be a valuable tool that permits to determine gross parameters of the HF radiator in an earthquake source with an explicitly specified accuracy.

ACKNOWLEDGMENT

Authors are indebted to anonymous reviewer and Dr H. Sato for valuable criticism and useful suggestions that greatly improved the manuscript.

REFERENCES

Ammon, C.J. *et al.*, 2005. Rupture process of the 2004 Sumatra-Andaman earthquake, *Science,* **308,** 1133–1139.

Guilbert, J., Vergoz, J., Schissele, E., Roueff, A. & Cansi, Y., 2005. Use of hydroacoustic and seismic arrays to observe rupture propagation and source extent of the $M_w = 9.0$ Sumatra earthquake, *Geophys. Res. Lett.,* **32,** L15310, doi:10.1029/2005GL022966.

Gusev, A.A., 1983. Descriptive statistical model of earthquake source radiation and its application to an estimation of short-period strong motion. *Geophys. J. Roy. Astr. Soc.*, **74,** 787–808.

Gusev, A.A. & Pavlov, V.M., 1978. A system of integral characteristics of earthquake source determined from far field body wave displacements, *Doklady AN SSSR,* **289,** 289–292.

Gusev, A.A. & Pavlov, V.M., 1988. Determination of space-time structure of a deep earthquake by means of power moments, *Tectonophysics,* **152,** 319–334.

Gusev, A.A. & Pavlov, V.M., 1991. Deconvolution of squared velocity waveform as applied to study of non-coherent short-period radiator in earthquake source, *Pure Appl. Geophys.,* **136,** 235–244.

Gusev, A.A. & Pavlov, V.M., 1998. Preliminary determination of parameters of the high-frequency source for the Dec 05, 1997 Mw = 7.9 Kronotsky earthquake, *XXVI Gen. Assembly, Eur. Seismol. Comission, Papers*, Tel-Aviv, Israel, 73–77.

Ishii, M, Shearer, P.M., Houston, H. & Vidale, J.E., 2005. Extent, duration and speed of the 2004 Sumatra–Andaman earthquake imaged by the Hi-Net array, *Nature,* **435,** 936, doi:10.1038.

Kakehi, Y. & Irikura, K., 1996. Estimation of high frequency wave radiation areas on the fault plane by the envelope inversion of acceleration seismograms, *Geophys. J. Int.,* **125,** 892–900.

Kruger, F, & Ohrnberger, M., 2005. Tracking the rupture of the Mw = 9.3 Sumatra earthquake over 1,150 km at teleseismic distance, *Nature,* **435,** 937–939.

Lay, T. *et al.*, 2005. The great Sumatra-Andaman earthquake of 26 December 2004, *Science,* **308,** 1127–1133.

Lomax, A., 2005. Rapid estimation of rupture extent for large earthquakes: application to the 2004, M9 Sumatra-Andaman mega-thrust, *Geophys. Res. Lett.,* **32,** L10314, doi:10.1029/2005GL022437.

Nishimura, T., Nakahara, H., Sato, H. & Ohtake, M., 1996. Source process of the 1994 far east off Sanriku earthquake, Japan, as inferred from a broad-band seismogram, *Sci. Rep. Tohoku Univ.,* **34,** 121–134.

Ni, S., Kanamori, H. & Helmberger, D., 2005. Energy radiation from the Sumatra earthquake, *Nature,* **434,** 582.

Stein, S. & Okal, E.A., 2005. Speed and size of the Sumatra earthquake, *Nature,* **434,** 581–582.

Tolstoy, M. & Bohnenstiehl, D.R., 2005. Hydroacoustic Constraints on the rupture duration, length, and speed of the great Sumatra-Andaman earthquake, *Seismol. Res. Lett.,* **76,** 419–425.

Tsai, V.C., Nettles, M., Ekström, G. & Dziewonski, A.M., 2005. Multiple CMT source analysis of the 2004 Sumatra earthquake, *Geophys. Res. Lett.,* **32,** L17304, doi:10.1029/2005GL023813.

Zeng, Y., Aki, K. & Teng, T.-L., 1993. Mapping of the high frequency source radiation for the 1989 Loma Prieta Earthquake, California, *J. Geophys. Res.,* **98,** 11 981–11 993.

APPENDIX: MINIMIZING FLUCTUATIONAL NOISE BY PREWHITENING

When planning data processing of signals of observed HF power or squared amplitude, one has to take into account that such a signal is significantly distorted by fluctuational noise. Thus one should try to reduce this noise as far as possible. Let us consider the data model in a certain time interval Δt (that corresponds to the temporal bin size in our actual processing) as a segment of stationary Gaussian 'noise' $x(t)$ with power spectrum $P(f)$, band-limited within the band $[f_1, f_2]$ ($f_1 = f_0 - \Delta f/2, f_2 = f_0 + \Delta f/2$). Consider Fourier spectrum $X(f)$ of $x(t)$, calculated over the duration Δt, at discrete points with step $\delta f = 1/\Delta t$ over frequency axis. Within the frequency band $[f_1, f_2]$, $X(f)$ includes $\Delta f/\delta f = \Delta f \Delta t = N_0$ statistically independent complex numbers. At a certain discrete frequency f_j within Δf, the mean value of $|X_j|^2 = |X(f_j)|^2$ is $P(f_j)\Delta t/2$. Both real and imaginary parts of X_j are independent random Gaussian variables with zero mean and variance $\sigma_j^2/2 = P(f_j)\Delta t/4$. Hence, each of N_0 values of $|X_j|^2$ is a χ^2_2, or equivalently, exponential random variable, of mean σ_j^2 and variance σ_j^4. It is now easy to determine mean μ_E and variance σ_E^2 for the observed total 'energy' $E = \int_0^{\Delta t} x^2(t)\mathrm{d}t = 2\int_{f_1}^{f_2} |X(f)|^2\,\mathrm{d}f$ in the band Δf over time Δt, and to derive the relative error of this estimate, or its coefficient of variation $CV_E = \sigma_E/\mu_E$. Derivation gives:

$$CV_E = \frac{\left[\sum P^2(f_j)\right]^{0.5}}{\sum P(f_j)} \quad . \tag{A1}$$

Considering the realistic case of sufficiently large N_0, one can rewrite this approximately as

$$CV_E = \left(\frac{1}{\Delta t^{0.5}}\right)\left\{\frac{\left[\int P^2(f)\mathrm{d}f\right]^{0.5}}{\int P(f)\mathrm{d}f}\right\}, \tag{A2}$$

where the factors representing the effects of bin size and of power spectral shape are separated.

An evident way to minimize CV_E is to increase bin size Δt; but wide bins mean badly resolved time history, and it is desirable to set Δt as low as possible. The second factor in (A2) is minimized by $P(f) = \text{const}$, that is, by noise that is white over Δf. Thus, to optimize processing one should pass the data trough the well-known 'pre-whitening filter', whose transfer function is proportional to the inverse of amplitude spectrum of the signal. As the source acceleration spectrum in the 0.5–5 Hz range behaves approximately as f^0, to achieve desired pre-whitening it is sufficient to convert the recorded signal to source acceleration. As a negative side effect, however, the values of 'energy' E and, therefore, 'power' time histories shall represent the time histories of power proper (that would use squared *velocity*) only with some distortion. This distortion however will be limited for the realistic case of octave frequency band and smooth mean spectral shape $P(f)$. We believe that the attained gain in information content justifies such a distortion.

Now let us consider numerical examples. We can measure information content by inverted variance, thus as the measure of information loss we use the relative increase of variance of the estimate of E, or RIV, with respect to the case of white noise or source acceleration signal: $RIV = [CV_E \text{ (case in question)}/CV_E \text{ (white noise)}]^2$. With (A2) we can determine RIV for model situations. For the particular frequency band 0.4–1.2 Hz, let us consider RIV for the following cases. (1) A raw P-wave velocity record, with $|X(f)| \propto \exp(-\pi f t^*) f^{-1}$. Setting $t^* = 0.8$, we find $RIV = 4.76$. (2) A similar attenuation-corrected record with $|X(f)| \sim f^{-1}$; then $RIV = 1.48$. (3) Both attenuation correction and conversion to acceleration is made; $RIV = 1$. Therefore, the information gain achieved by pre-whitening may be quite appreciable.